Environmental Science Advances

ROYAL SOCIETY OF CHEMISTRY

PAPER

View Article Online
View Journal | View Issue

Cite this: *Environ. Sci.: Adv.*, 2025, **4**, 1633

Pore size effects upon adsorption of PFAS in covalent organic frameworks: molecular dynamics study

Timothy C. Ricard, [ab] Timothy C. Schutt, [b] Caitlin G. Bresnahan [b] and Manoj K. Shukla*[b]

Per- and polyfluoroalkyl substances (PFAS) are a large class of industrial chemicals whose diversity, spread, and environmental/health impacts have recently become a major concern for environmental and health policy makers. This concern is further exacerbated by their pervasiveness and chemical resilience, which complicates their removal from watersheds and other contaminated environments. Due to the chemical stability of the carbon–fluoride bonds, they are difficult to degrade. Instead, an alternative presents itself in the form of adsorption, concentration, and then removal of PFAS from contaminated sites. Both metal organic frameworks (MOFs) and covalent organic frameworks (COFs) have recently come under significant investigation as possible adsorption media which could be adapted for the removal of PFAS from contaminated sites. To gain greater insight into the adsorption capabilities of COFs for the removal of PFAS from waterways, we have studied the adsorption of PFAS molecules in COFs of differing pores sizes using molecular dynamics simulations. We examine the absorption of aqueous PFBA, PFOA, and PFOS into Covalent Triazine-Based Frameworks (CTF) of different pore sizes. This mechanistic adsorption data shows that a goldilocks zone occurs in pores with diameters of around 8 Å where the PFAS thread through the pores smoothly. Kinetic factors from diffusion into these nanopores favors the adsorption of short chain PFAS even though larger PFAS are thermodynamically favored. Each pore tends to initially adsorb only one PFAS, occupying the mouth of the pore, until the local COF surface is saturated and then multiple occupancy per pore can occur. Discussion on the impacts of PFAS concentration and interaction with the pores will inform design principles for enhanced selectivity and capacity for PFAS adsorbent material.

Received 18th December 2024
Accepted 5th August 2025

DOI: 10.1039/d4va00422a

rsc.li/esadvances

Environmental significance

The spread of per- and polyfluoroalkyl substances (PFAS) in global waterways has become a subject of significant concern. In this manuscript we explore the adsorption of perfluoroalkyl substances (PFAS) into covalent organic frameworks (COFs) for the purpose of improved environmental remediation. The paper provides computational insights into the impact of pore size of COFs upon their adsorption of linear PFAS from an aqueous environment. The mechanistic adsorption results indicates that a "goldilocks" diameter of 8 Å allows for smooth adsorption of the target linear PFAS. Furthermore kinetic factors favor the shorter chain PFAS while the longer chain PFAS are thermodynamically favored. Mechanistic insights from this work can help inform the design principles for selectivity and capacity for PFAS adsorption into porous materials.

1. Introduction

In the last few decades, the presence of fluorocarbons in the environment, especially in water reserves, have become a significant cause for concern as they span an extremely broad range with regard to toxicity.[1–6] United States Environmental Protection Agency (USEPA) has identified a number of PFAS to control and regulate due to their potential health, and environmental risk concern.[7,8] It should be noted that shorter chain analogues, such as perfluorobutanoic acid (PFBA), are increasingly substituted for their longer chain cousins, thus are becoming more prevalent in wastewater and waterways.[9,10] These acids are part of the larger class of poly- and perfluoro alkyl substances[11,12] (PFAS) which can often behave as surfacants. Their use for water-proofing and oil proofing in the textile, leather, and paper industries and their use in fire suppression,[13,14] due to their nonflammable and noncorrosive character,[15] lead to large scale contamination of waterways and soils.[16–18] This contamination of waterways and soils poses large

[a]*Oak Ridge Institute for Science and Education, 1299 Bethel Valley Road, Oak Ridge, Tennessee 37830, USA*

[b]*Environmental Laboratory, US Army Engineer Research and Development Center (ERDC), Vicksburg, Mississippi 39180, USA, Manoj.K.Shukla@usace.army.mil*

ecological and human health threats[1,2,4,5,12] as due to their tendency to bioaccumulate.[15,16,19,20] This bioaccumination and the widespread nature of PFAS contamination leads to systematic maladies such as thyroid[21] and kidney diseases,[22] infertility,[23,24] and a host of cancers.[25–27]

PFAS are amphiphilic substrates as they have hydrophilic functional groups, such as the carboxylic group (in PFOA and PFBA) or sulfonic group (in PFOS), and a hydrophobic fluorinated tail of variable length. The fluorination of hydrocarbon-based amphiphiles has allowed for a more diverse and tailorable use of this class of molecule.[28–30] The fluorination of organic chains, which provide the hydrophobic portion of many amphiphiles, offers longer and more stable bonds as compared to the hydrocarbons.[11,31,32] These bonds are also less polarizable and, compared to hydrocarbon bonds, the C–F bond has reverse dipole moment, which can lead to fluorinated organic molecules becoming more hydrophobic while offering similar steric and conformational conditions.[2,33,34] These amphiphilic properties and the chemical stability of the many members of the PFAS class of chemicals poses a significant problem for remediation efforts. There has been a large number of different approaches towards the collection and removal of PFAS from contaminated aqueous and soil environments. A variety of materials have been considered as adsorption media including biochar,[35–38] graphene,[39–41] functionalized clays,[42–44] ion exchange resins,[45–47] porous organic polymer networks,[48,49] and activated carbon.[50–52] Unfortunately, many of these adsorbent media struggle with competitive adsorption of miscellaneous coexisting organic matter in waste water. Activated carbons (AC) has been the default sorbate for removal of PFAS from contaminated soils, due to their high surface area, large binding capacity, and high removal effectiveness, but they suffer from relatively slow adsorption rates and require frequent replacements.[53,54] AC relies on hydrophobic interactions with the fluorocarbon tail while the hydrophilic headgroup interacts with the polar solvent. Thus most AC formulations, along with other hydrocarbon sorbates, are optimal for longer chain PFAS adsorption, but struggle to capture shorter chains, due to their lower hydrophobic character. Additionally, PFAS with sulfonic head groups, such as PFOS, are oleophobic, thus struggle to adsorb to hydrocarbon surfaces like activated carbon.[55] In contrast, ion exchange resins, another common sorbent for the removal of PFAS, relies on interactions with the charged head group rather than the hydrophobic tail. Due to diffusion rates, ionic exchange shows higher adsorption performance for shorter chain PFAS over their longer chain cousins during to difficulty with diffusion.[56] Thus ion exchange flips the efficiency as compared to AC, better with short chain but worse with long chain PFAS. One major draw back for ion exchange is the presence of inorganic ions can significantly reduce sorption effectiveness.[57]

One promising alternative avenue is the use of materials with permanent hydrophobic pores which could take advantage of the amphiphilic nature of PFAS, combining the advantages of the hydrophobic character of AC and interactions with the ionic head as done with ion exchange. As such, both metal organic frameworks (MOFs)[58–61] and covalent organic frameworks (COFs)[62–65] are promising classes of materials which could prove useful for PFAS remediation. COFs were established by the seminal work of Yaghi and co-workers in 2005 (ref. 66) as a new class of nanomaterial which has shown great promise for adsorption of diverse classes of pollutants.[65,67,68] MOFs[69–73] and COFs[74–77] have been studied to this end, and have proven to show promise for remediation efforts. These organic frameworks have a number of advantages, such as having a regular pore structure and adjustable functional groups for tailoring of the local chemistry.[65,78] COFs offer additional advantages over MOFs in that they are more stable in harsh environments, having higher thermal stability, lower mass density, and maintaining permanent microporsity.[67]

Unfortunately a number of popular COFs are boron-based which means that they have decreased chemical stability in moist and aqueous environments.[62] Therefore, in this work we will consider covalent triazine-based frameworks (CTF) which are constructed by the cylcotrimerization of aromatic nitrile monomers, and are thus stable in aqueous settings.[79–81] The added advantage of CTF is that environmentally inert $ZnCl_2$ can be used as both as a liquid ion solvent and catalyst, and the constituent monomers are cheap and abundant. Work done by Wang *et al.*[82] established that a triazine based COF, CTF-1, showed promise for the adsorption of linear PFAS. They found that the adsorption affinities and capacity of CTF-1 for longer chained PFAS out performed AC, single walled nanotubes, and resins. This higher adsorption affinity is explained by both electronic static interactions with the nitrogens of the azines and the hydrophobic interactions with its conjugated rings, both interactions driving PFAS into the pores of CTF-1. Other work on CTFs and related triazine macro-structures have confirmed the efficacy triazine as a chemically stable linker which helps induce PFAS adsorption.[48,49,83–85]

The past performance of triazine-based frameworks gives a good avenue to build upon the ideas suggested in a study by Erkal *et al.* which examined the impact of pore size of MOFs upon their effectiveness for PFOA adsorption.[73] Their study indicated that pore diameters below 6 Å are too narrow, and that their optimal pore size may be between 8–10 Å. Thus, in this work we considered three CTF systems over the aforementioned range of pore sizes; these pores present a principally hydrophobic environment,[86] but with nitrogen as a hydrogen bonding recipient for the charged, hydrophilic head groups. The three CTF systems considered in this work in increasing order of pore diameter are: CTF-FUM (5.6 Å),[80] CTF-1 (8.0 Å),[79] and CTF-2 (10.1 Å).[81] In order to investigate the impact of the pore size upon PFAS adsorption we considered the dilute limit of an adsorption of a single PFAS into the pore, and concentration studies with mixed PFAS using molecular dynamics simulation. We found that the optimal pore size is approximately 8.0 Å and CTF-1 is found to be the most effective of the three COFs modelled for adsorption and retention of PFAS contaminates in an aqueous environment. CTF-1 inhabits the goldilocks zone between the steric hindrance of the smaller pores (CTF-FUM) and the reduction of hydrophobic driven adsorption with the increase of pore size (CTF-2). This further substantiates the previous work done by Deng and Liao on CTF-1 effectiveness giving

atomistic level understanding of the mechanisms of PFAS adsorption to these triazine based COFs. In Section 3 we discuss the construction and composition of the systems, and the details of the umbrella sampling and molecular dynamics simulations. In Section 4.1 the results of the umbrella sampling simulations are considered, and in Sections 4.2 and 4.3 the features of the molecular dynamics simulations are discussed. Finally in Section 5 we summarize our results and present the implication for the design of PFAS adsorbents.

2. Method

In this study we consider three covalent triazine-based frameworks (CTF), a family of COFs, with varying pore diameters in order to gauge their ability to adsorb PFAS contaminates. This allows for the consideration of pore size effects while maintaining a similar chemical environment within the pores. The CTFs are represented as finite covalent macromolecules with a 4×4 pore configuration. The three COFs considered in this work are shown in Fig. 1, the precursor monomers are shown in the SI. This pore configuration provides ample number of pores to be sampled. Three different species of PFAS were selected to represent the major characteristics of common PFAS contaminates posing environmental concerns. Firstly PFBA, Fig. 2(a), was chosen to represent short chain species which are well known to be resistant to capture, but are also common products of many degradation methods and pathways.[87,88] Next PFOA and PFOS, Fig. 2(b and c), are considered in order to present longer chain PFAS which are common primary contaminates. Both species have well documented impacts on human health.[1–5] These species also represent the two most common head groups within the PFAS family: carboxylic and

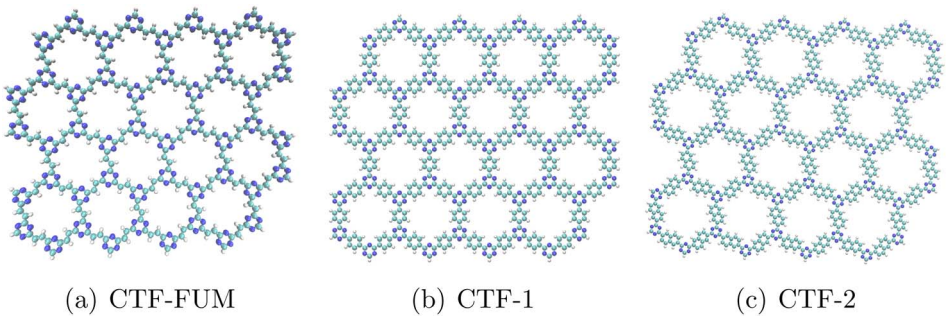

Fig. 1 Illustration of the structures of the 3 COFs considered in this study: (a) CTF-FUM, (b) CTF-1, (c) CTF-2.

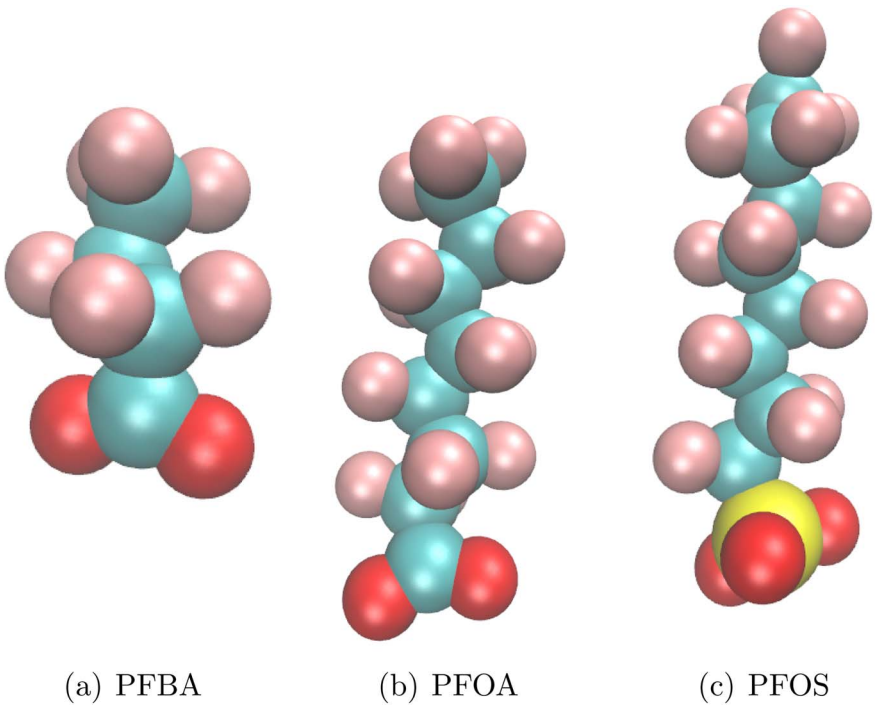

Fig. 2 Common contaminant PFAS species chosen to represent the broad characteristic of linear members of the PFAS chemical family: (a) PFBA, (b) PFOA, (c) PFOS.

Table 1 Concentrations (in molality) chosen for each MD simulation

COF	30PFAS	45PFAS	75PFAS
CTF-FUM[80]	0.035	0.053	0.092
CTF-1 (ref. 79)	0.031	0.048	0.083
CTF-2 (ref. 81)	0.031	0.048	0.083

sulfonic acid. Given that our goal is to remove these species from standard environmental conditions, they are only to be considered in their anionic form which is dominate for pH > 3.7.

Molecular dynamics (MD) simulations and umbrella sampling implemented in the Amber20 software package[89] were used in the present investigation. Initial coordinates were created using packmol[90] and stabilized through 2000 steps of conjugated gradient followed by 2000 steps of steepest descent minimization. Equilibration of the density was carried out using the Brendensen barostat and Langevin thermostat set to 1 atmosphere and 300 K respectively for 1.2 ns of simulation time. This is triple the time it took for systems to initially reach full density. These optimized systems were then used for umbrella sampling (3.1) and molecular dynamics simulations (3.2). TIP4P-EW water model[91–93] was used for the solvent and general amber forcefield (GAFF) parameters defined the bond, angle, dihedral, and Lennard-Jones terms of each PFAS molecule.[94] The electrostatic point charges on anionic PFOA, PFBA, PFOS were calculated from restrained electrostatic potential mapping implemented in antechamber[95] based on the underlying electronic distribution calculated in Gaussian 16 at HF/cc-PVDZ for each molecule.[96–99] This assignment of charge has been shown not to require post-assignment scaling to produce quality results.[100] Ten layers of the model COF macromolecules were stacked vertically on top of each other with direct alignment to form pores that are about 33 Å in length. Initial COF structures were obtained from CoRE COF Database.[101] Graphical representations of molecules and molecular figures were created with the program VMD.[102]

2.1. Molecular dynamics umbrella sampling methods

Umbrella sampling simulations were employed to derive the potential of mean force (PMF) for PFAS adsorption and transport through the pores of each COF. Initial placement of the PFAS molecule was set to be inside an inner pore of COF cell structure. Steered MD was employed to get initial frames along the reaction coordinate in both directions coming into and out of the pore. The collective variable for this umbrella sampling is the projection of the vector between the head group of the PFAS and the center of an interior pore onto the vector parallel to the long axis of the pore. Starting frames were taken from along the reaction coordinate from −40 Å to +40 Å away from the center of the pore in 1 Å increments. These frames used with a harmonic restraining potential of 1 kcal mol^{-1} $Å^{-1}$ to sample each window in the umbrella sampling for 1.0 ns. Biases for each window were used to only constrain the displacement along the vector parallel to the axis of the roughly cylindrical pores, while the degrees of freedom perpendicular to the pore were left unconstrained within the dynamics. Weighted Histogram Analysis Method (WHAM) was used to integrate energy differences between each window into PMF curves across the whole reaction coordinate. Periodic boundary conditions were enforced in both the simulation and PMF calculations so that local environment in the bulk water above and below the pore would match. Convergence of the PMF was checked by looking at the first and second halves of the window data individually, each producing a PMF no more than 5% different from the overall PMF calculated from the total data. Pore radii of each COF were

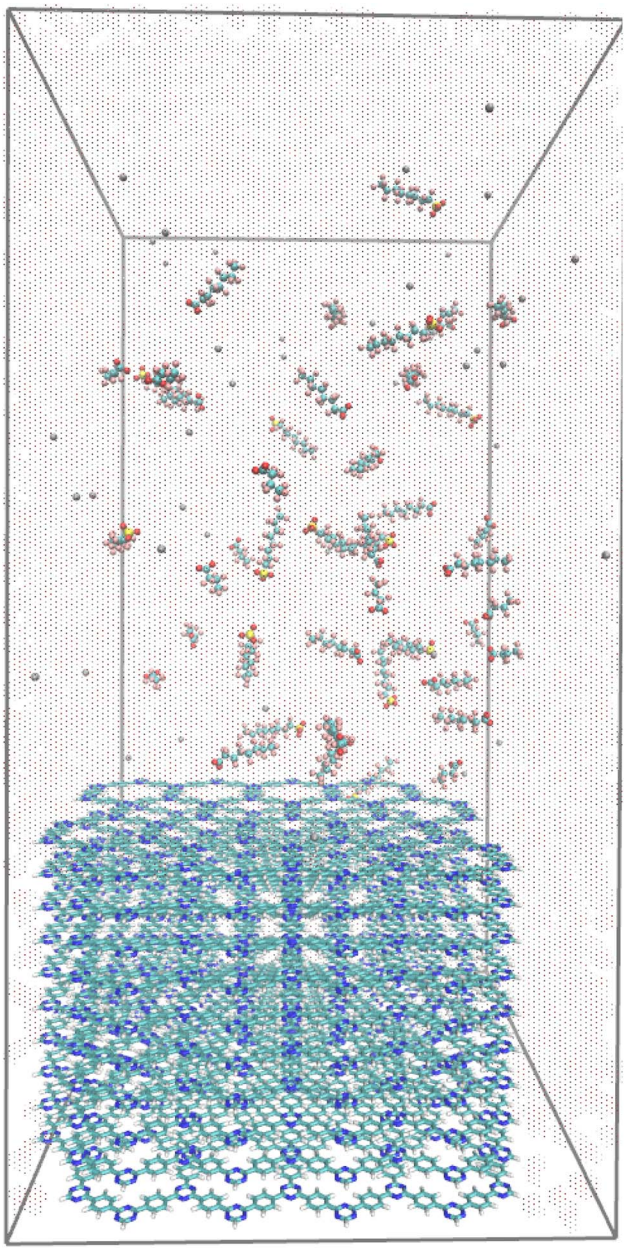

Fig. 3 Initial system set up before optimization and equilibration. Components: 10 COFs stacked, equal counts of each PFAS species (see Table 1) with Na^+ as counter ion, solvated with water.

calculated as the largest sphere that could fit through the most constrictive part of the pore.

2.2. Molecular dynamics trajectories with varied PFAS concentrations

Molecular dynamics simulations were employed to explore the free energy and statistics of PFAS adsorbing into the pores of the target COFs under standard environmental conditions. Concentrations of the solute PFAS species were varied across simulations with 5 replicate trajectories calculated for each concentration and COFs selection, the concentrations for each set of replicas is shown in Table 1. These deprotonated PFAS molecules were randomly packed into the aqueous phase with equal counts of PFBA, PFOA and PFOS with appropriate number of Na^+ to neutralize the overall charge of the simulation box. An example pre-optimized system is illustrated in Fig. 3. The concentrations are reported in Table 1 are in molality as the systems were equilibrated in an isothermal-isobaric ensemble, while the production is isochoric, thus the effective volume varies mildly between trajectories making the Molarity variant between trajectories. Such high concentrations were used in order to efficiently sample what happens as the surface capacity of the COF is reached and exceeded. The production simulations were run under the canonical ensemble within isochoric, periodic boundaries over 100 ns with a 2 fs time step at 300 K. Structural configurations were recorded every 5000 steps, which is 10 ps, for analysis in each trajectory. This sampling rate lead to 10 000 snapshots per trajectory.

3. Results and discussion

In this investigation, we have considered the adsorption and retention of aqueous PFAS into COFs of varying pore diameters. Fig. 4 illustrates (a) the 4×4 layout of pores considered in this study and (b) an example of PFAS adsorption into these pores. In order to first examine the dilute limit of a single PFAS molecule adsorbing into each COF, in Section 4.1 we consider umbrella sampling to ascertain the energetic landscape for a single PFAS molecule to traverse the pore. Subsequently, we performed molecular dynamics simulations with varying PFAS concentrations to determine collective interaction energies (Section 4.2.1), saturation and retention (Section 4.2.2), and geometric distributions (4.3) of the PFAS species with the 3 different COF systems at various concentrations. We finish with a brief conclusion recapitulating the implications for PFAS adsorbent design.

3.1. Adsorption and transport of dilute PFAS in COF pores

Umbrella sampling simulations of individual PFAS molecules going through the COF pore structure were employed to deliberately sample each stage of entering and exiting pore spaces in the absence of compounding factors from co-adsorption, aggregation, or other effects. The resulting PMF from integrating these umbrella sampling simulations is shown in Fig. 5. In CTF-1, panel C of Fig. 5, there are very clean delineations between each regime. First regime is from −40 Å to −27 Å where the PFAS is completely solvated in the water phase. Second regime is from −27 Å to −15 Å where the PFAS molecule gradually increases their interaction with the COF surface and the fluorocarbon tail begins to thread into the pore. It is worth noting that without any imposed bias to the orientation of the PFAS, across all PFAS systems it was seen that the hydrophobic tail of the PFAS would interact with the COF and pore before the head group would reach the COF interface. Third regime is from −15 Å to 3 Å where the PFAS molecule is completely contained within the pore. Fourth regime is from 3 Å to 15 Å where the tail of the PFAS molecule begins to protrude out of the pore while the headgroup is still inside. Fifth regime is from 15 Å to 27 Å where the head group emerges from the COF pore while its tail has first increasing, then decreasing interaction with the COF surface while the molecule flips around. And the final regime is from 27 Å to 40 Å where the PFAS is once again completely solvated by water away from the COF. When the PFAS molecule is within the 8.0 Å pore of CTF-1 there is a flat potential well of −10 kcal mol^{-1}, −24 kcal mol^{-1}, and −28 kcal mol^{-1} for PFBA, PFOA, and PFOS respectively. These are significant thermodynamic energies driving adsorption of the PFAS from the aqueous phase into the COF. Across all three COFs tested there are some conserved features in the PMF. Firstly, the potential energy wells around a distance value of 21 Å are where the PFAS molecule is flat atop the COF surface maximizing tail-COF hydrophobic interactions as much as possible without entering the pore. In this configuration the head group comes just off the plane to become solvated by water. Secondly, the most favorable distance across the free energy profile for each PFAS tested occurs at a distance of −15 Å. At this distance, the tail is fully enclosed in the COF pore and the head group is poking out just enough for both oxygen atoms to form hydrogen bonds with water. It should be noted that in the larger-pore COFs, CTF-1 and CTF-2, a single water follows the PFAS through the pore maintaining a hydrogen bond with the anionic oxygen continuously. Full solvation of the headgroup is prohibited sterically by the pore walls.

CTF-FUM and CTF-2 have more complicated PMF curves than CTF-1 in the domain where the PFAS is within the pore. In the case of CTF-FUM, panel B of Fig. 5, variances in the range of −15 Å to 3 Å are due to constriction in the pore. These constrictions in the pore exclude water from wetting the interior and increase the interactions of conjugated walls with the anionic head groups as the molecule gets deeper in the pore. These constriction points also limit the flexibility of each PFAS causing a propensity for higher energy configurations that can disfavor the PFAS entering deeper into the pore. At the mouth of the pore is the highest opportunity for PFAS binding to CTF-FUM with thermodynamic energies of −8 kcal mol^{-1}, −19 kcal mol^{-1}, and −13 kcal mol^{-1} for PFBA, PFOA, and PFOS respectively. In general, the adsorption energies for PFOS are similar to those of PFOA but not in the case of CTF-FUM. This is due to the larger sulfonate head group having steric limitations within the small 5.6 Å pores. The PMF curves for CTF-2 are shown in panel D of Fig. 1. Interestingly, here we see the PFBA PMF is effectively identical for both sides of the pore coming in or out. This is because the pore diameter, 10.1 Å, is large enough

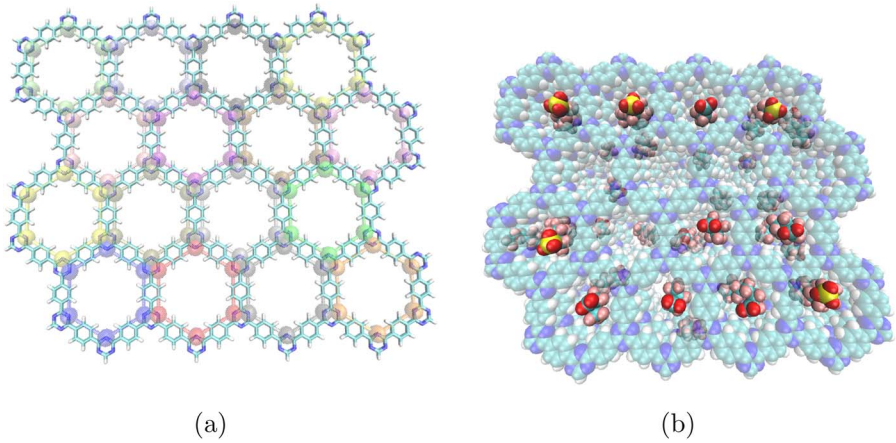

Fig. 4 COF model subsystems considered have a 4 × 4 staggered pore topology. (a) Displays this 16 pores for a single layer of CTF-1. (b) Illustrates an example 10 layered CTF-1 membrane with adsorbed PFAS species in these pores. Table 2 shows the pore sizes for the three COFs considered within this work.

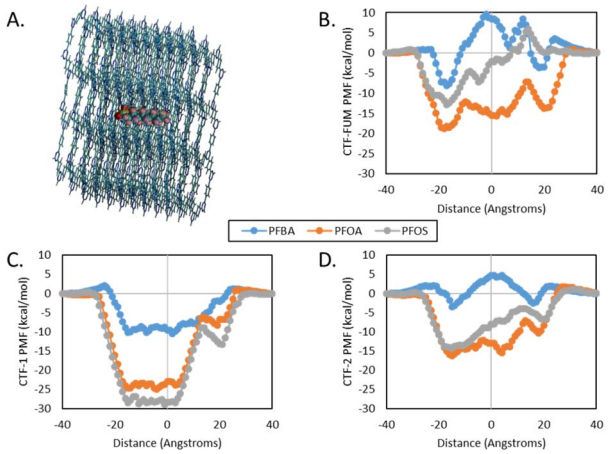

Fig. 5 Umbrella sampling pulling PFAS molecules through COF pores. Blue is for PFBA, orange is for PFOA, and gray is for PFOS. (A) Panel A shows the system set up with PFAS in a central pore, (B) panel B shows the PMF curves for CTF-FUM with a pore size of 5.6 Å, (C) panel C shows PMF curves for the CTF-1 with a pore size of 8.0 Å, and (D) panel D shows PMF curves for CTF-2 with a pore size of 10.1 Å.

to permit the short chain alkyl group to flip around regardless of starting or entry orientation. Thus, on both sides of the COF we see minima where the hydrophobic tail group is inside the pore and anionic head exposed to the bulk water. Perturbations from this minimum increases the thermodynamic energy as either the head group gets drawn into a hydrophobic region (−15 Å to 15 Å) or as the tail group is pulled away from the COF (<−16 Å or >16 Å) into the bulk water phase, either way resulting in less favorable interactions compared to right at the mouth of the pore.

The variances between the PMFs can be examined by analyzing each window individually to determine some of the underlying driving factors and interactions. Fig. 6 shows data for each of the 3 PFAS with each of the 3 COF structures in regard to the average angle of the PFAS relative to the pore, average total interaction energies, interaction energy component from water, and interaction energy component from the COF. Each point represents the average of 1 ns of data in each window. Fig. 6 panel A shows the average angle of each PFAS relative to the pore axis as a function of displacement through the pore (Fig. S2 in the SI illustrates this angle). When looking at z-displacement of −27 Å to −40 Å and 16 Å to 40 Å, the average angle ranges from 45° to 135°. These values indicate a relatively random orientation of the PFAS when it is located in bulk water. Once PFOA and PFOS move into the pore (from −27 Å to 15 Å)

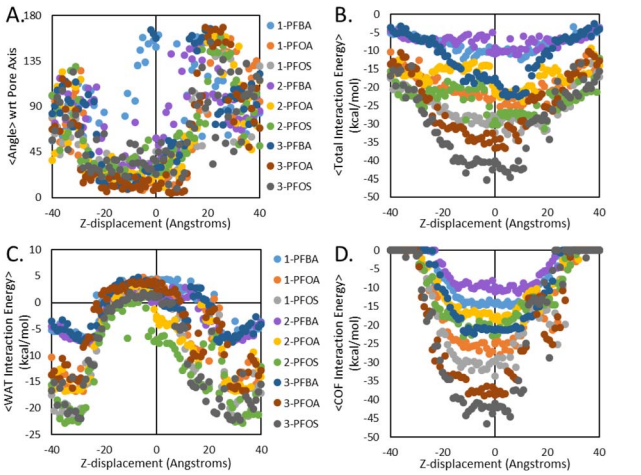

Fig. 6 Scatter plots for the for each PFAS type in as a function of distance from the pore center for each COF pore averaged over the simulation trajectory. (A) Panel A shows the averaged angle of the long axis of each PFAS from head to tail with respect to the pore axis, (B) panel B shows the average total interaction energy of each PFAS with the environment around it as a function of distance from the center of the pore, (C) panel C breaks down the component of interactions between PFAS and water as a function of distance from pore center, and (D) panel D shows the interaction energy component between PFAS and COF as a function of distance from pore center. Illustration of how the angles are defined in shown in the SI.

there is a strong axial alignment. This randomness is observed in the aqueous phase outside the pore; but as soon as PFOA or PFOS are into the pore, from −27 Å to +15 Å there is a strong axial alignment. Naturally the larger diameter pore, CTF-2, has more variability in the angle as can be seen in Fig. 6 panel A. Interestingly, PFBA shows the ability to flip around inside the pores of even the smallest COF here, CTF-FUM. Between displacements of 15 Å to 27 Å there is a forced flip of the PFOA and PFOS molecules. As the hydrophobic tail group protrudes from the pore, as much as steric interferences allow, the molecule favors aligning perpendicular to the pore and parallel to the COF surface. Meanwhile, as the molecule begins to exit the pore, it flips around so that the head group faces the aqueous phase, and tail group remains within interaction range of COF. This phenomena where PFAS flips around is associated with an extra energy barrier when PFAS are entering or exiting the COF's pore. This can be seen in the PMF (Fig. 6 panel A) and the interaction energy (Fig. 6 panel B) curves. Importantly, this means that without bias driving forces, the PFAS will never pass all the way through COF pores of these diameters, but rather favor occupying the mouth of each pore where the COF interfaces with water. Implications of this trend include a high adsorption sensitivity to particle size/surface area. Fig. 6, panels B–D show the linear interaction energy (LIE) associated with interactions between each PFAS and the total system, the aqueous component, and the COF component respectively. The calculation of LIE is discussed in more detail in the next section. Whereas the PMF curves are much higher resolution due to WHAM integrations, the LIE curves have the advantage of being able to deconvolute the component contributions. Both the water-PFAS and COF-PFAS LIE curves highlight the energy penalty of the aforementioned flipping-around mechanism of the PFAS molecule that occurs between displacements of 15 Å to 27 Å. Overall LIE curve sorption stability show that PFAS interactions with the COF follow the trend PFBA < PFOA < PFOS. Furthermore, the PFAS have the strongest interaction with CTF-FUM, followed by CTF-1, and then CTF-2. In other words, the smaller the pore, and the larger the PFAS molecule, the more LIE is expected to be observed. One practical implication of this observation is that, even at these small pore sizes, the adsorption of short chain PFAS will not be thermodynamically preferred over longer chain PFAS. Thus, COF adsorption for PFAS removal may make the most sense as a final cleaning step. The COFs under analysis herein have a strong affinity to remove PFAS at dilute concentrations, but lack the specificity for hard-to-remove short chain PFAS.

Table 2 Theoretical partitioning of aqueous PFAS on COF substrates at 300 K predicted from umbrella sampling energies

COF	CTF-Fum	CTF-1	CTF-2
Pore size	5.6 Å	8.0 Å	10.1 Å
log(K_{cw})partitioning			
PFBA	−5.9	−7.7	−2.6
PFOA	−13.7	−18.3	−11.8
PFOS	−9.4	−21.1	−10.4

The predicted initial partitioning coefficients in Table 2 highlight the thermodynamic preference for aqueous PFAS to adsorb into COF pores (expression shown in the SI). These partitioning coefficients, K_{cw}, between the COF and water states were calculated using the energies from the umbrella sampling normalized by assuming Boltzmann populations. For example, for PFBA in CTF-1 pores the log(K_{cw}) value of −7.7 means that a PFBA exposed to an empty pore is 50 million (*i.e.* $10^{-7.7}$) times more likely to adsorb into the pore rather than remain solvated in the aqueous phase. Unsurprisingly, the short chain molecules like PFBA are more difficult to adsorb than longer chain analogues owing to the decreased degree of hydrophobicity driving them out of solution. Of the COFs in Table 2 it is clear that CTF-1 will be the best material for refining dilute systems of PFAS down below non-detect limits. Since each COF in this set has essentially the same chemistry, just with a differing pore size, we can conclude that near 8.0 Å is the optimal size for the highest thermodynamic affinity of PFAS. Pores as small as 5.6 Å discourage PFAS entry through steric and capillary effects. While pores as big as 10.1 Å lose the ability to host hydrophobic interactions around all sides of the PFAS chain in favor of water filling that gap. Furthermore, radial density functions of water with the pore nitrogens and statistics of the water hydrogen bonding with these nitrogens, shown in Fig. S10, show the hydrophobic character of the pores. In particular, CTF-1 was shown to interact the least with water molecules and instead favor PFAS adsorption.

It must be noted that initial log partitioning coefficient values in Table 2 do not take into account the impacts of concentration. Complexities from features of COF adsorption devices such as particle morphology, aggregation, and processing variables make the concentration effects difficult to evaluate quantitatively *in silico* predictions. That said, synergistic binding and aggregation can be investigated using MD of PFAS-concentrated systems.

3.2. Saturation of CTF pores by aqueous linear PFAS

Molecular dynamics simulations were run for 5 replicates across 3 concentrations for each CTF structure studied. These dynamics trajectories allows for the incorporation of PFAS cooperative and inhibiting interactions, kinetic and time scale effects, and a larger sampling of the free energy surface than what can be found in more targeted approaches.

3.2.1. Linear interaction energy between PFAS and the COF subsystems. Linear interaction energies (LIE) showcase the sum of non-bonded interactions, electrostatics and van der Waals, between two species. In Fig. 7, the LIE is plotted with respect to PFAS species and concentration showing an increasing trend with size of the sorbate molecule, and decreasing trend with concentration. On a per-mole basis the larger PFAS molecules unsurprisingly have more interaction with the sorbent than the short chain. More specifically, PFOA and PFOS behave with nearly equivalent interaction strengths and each are approximately double the interaction of PFBA with the COFs. In the smallest pores of CTF-FUM there is large uncertainty derived from the standard deviation of the LIE results across the

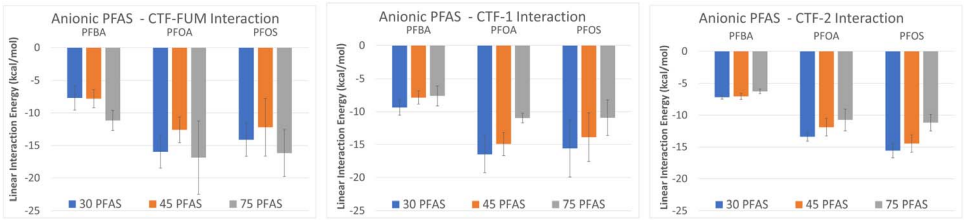

Fig. 7 Linear interaction energy of between the anionic PFAS and the COF subsystems: (a) CTF-FUM, (b) CTF-1, (c) CTF-2.

replicates. This uncertainty arises from the steric difficulty of accessing such small nanopores. Once, and if, the molecules do get inside the pore, the binding interaction is strong. However, the variability in threading into the pore *vs.* laying across the surface *vs.* remaining in solution leads to a wide range of potential equilibrium average binding across the whole set of PFAS molecules in the box. Due to the statistical uncertainty, it is difficult to extract trends with respect to concentration in the CTF-FUM system. In CTF-1 and CTF-2 there is a notable, albeit uncertain, trend where the higher concentrations of PFAS have an overall decrease in the average interaction energy of each species. As the first PFAS molecules reach the COF, they bind in the most favorable configurations occupying the mouth of each pore. As additional PFAS diffuse around the COF surface, the binding locations available are still favorable. However, these spaces are less favorable than the pore mouth locations that are already occupied were for the first few PFAS molecules. Intriguingly, regarding the concentration trend described above, the average interaction intensity of PFBA is impacted less than PFOA and PFOS by increased numbers of PFAS. This is because in these systems, which were run with all PFAS in the system simultaneously, it was seen that PFBA's greater motility causes it to kinetically outcompete the PFOA and PFOS for sorption. Consistent with the previous discussion (see Fig. 5 panel C and Table 2), the LIE results also highlight that CTF-1 exhibits stronger binding interaction than CTF-FUM or CTF-2 especially when it comes to binding of PFBA.

In order further investigate the binding of PFAS within the pores of the target COFs, we employed the thermodynamic integration for all of the bound PFAS in the final frame from single trajectory per COF. Thermodynamic Integration (TI) is a simulated analysis technique that gradually decouples a molecule from the rest of the simulation box. This occurs through the elimination of non-bonded interactions (van der Waals and electrostatics) and integrating the change in energy over the course of overlapping windows using a Gaussian quadrature distribution of the lambda values that weight the interaction intensity between 1 and 0.[103] As such, TI data explicitly accounts for solvation and system response to the absence of a molecule and is referred to as the Gibb's free energy of vaporization for that molecule. In comparison to LIE analyses, which account for the interactions between just two species as specified, the TI is comprehensive energy for a single molecule leaving the whole system. Averaged TI results, reported as the condensation energy (which is the negative of the vaporization energy), for PFAS that were bound to the COF are shown in Fig. 8.

From the TI results, it is again apparent that the longer chain PFOA and PFOS species have more interaction with the solvated COF system than PFBA. Also, in general, the extent of interaction is stronger for the smallest pore COF following CTF-FUM > CTF1 > CTF-2. The PFAS molecules are harder to vaporize or remove from the smaller pores. The only exception is PFBA with CTF-1 which vaporizes the easiest of all PFAS-pore combinations. This could be a result of uncertainty since the standard deviations of TI for PFBA in CTF-1 and CTF-2 overlap or it's possible this is a feature of that goldilocks pore size that PFBA threads so nicely into as seen in the following section.

3.2.2. Absorption and retention of PFAS in CTF pores. Molecular dynamics simulations were initiated with all of the PFAS molecules within the aqueous phase, as can be seen in Fig. 3 where the PFAS are "above" the 10 COF layers (It should be noted that this is a periodic simulation that the aqueous PFAS can and do diffuse into both sides of the 10 COF matrix). During the optimization steps of the system, discussed in Section 3.2, a few of the PFAS molecules absorb into the COF. The majority of the adsorption events occur within the early portions of the dynamics trajectory (See Fig. S3–S5). In order to classify whether a PFAS molecule was adsorbed into a particular pore, the terminal tail carbon of the PFAS must be within a distance cutoff of 4 of the 6 nitrogens which form the pore from the same layer. The distance cutoff chosen is determined

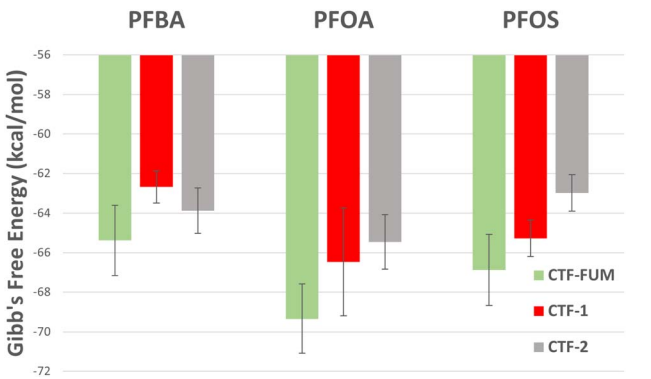

Fig. 8 Average Gibbs free energy of PFAS binding to the different COFs from thermodynamic integration.

by the distance between secondary neighboring (*meta* position) nitrogens within a pore for the given COF, as shown in Fig. 9. This cutoff and the effective pore volume is illustrated in Fig. 9. This criteria functions to capture the full pore volume without including double counting from adjacent pores. The terminal carbon was selected as to qualify whether the PFAS molecule is fully embedded in the COF layer. This is because, as discussed in Section 4.1, the all three species of PFAS are energetically favorable to enter the pore tail first and can be favorable for the head group to remain just out of the pore while remaining effectively bound and adsorbed in the COF layer.

During dynamics trajectories, the PFAS are reversibly adsorbed and desorbed back into the aqueous phase, so first we consider the fraction of time the average member of each species spends adsorbed in the 16 pores of the model COF systems. This analysis is done over 3 different PFAS concentrations as outlined in Table 1 in Section 3.2. Fig. 10 shows the fractional absorbance (time spent) by PFAS species for each of these three PFAS concentrations. Fractional adsorbance is the time-average of the total adsorption for every PFAS molecule of a given species in the simulation. Each COF was considered with 5 replicate trajectories at each concentration. All three COFs considered here show significant adsorption of all three species of PFAS. The larger pore COFs, CTF-1 and CTF-2, show approximately double the fractional adsorption at the lower concentration compared to the adsorption levels seen in CTF-FUM. At the lower concentrations, all three COFs showed no statistical preference towards any of three PFAS species. When the concentration increases there is still no appreciable difference in fractional adsorbance between the three species for the CTF-FUM and CTF-2 COFs. In contrast at the highest concentration CTF-1 demonstrates a higher adsorption fraction for PFBA than the longer chained PFAS, suggesting that CTF-1 may preferentially adsorb shorter chains such as PFBA. Additionally, there is no statistically significant impact the head group chemistry upon the fractional adsorption, which is consistent with the umbrella sampling and linear interaction energy results. As the concentration of all three species are increased, the shorter chained PFBA out-competed the other two and spent a disproportionately higher time in the COF pores as compared

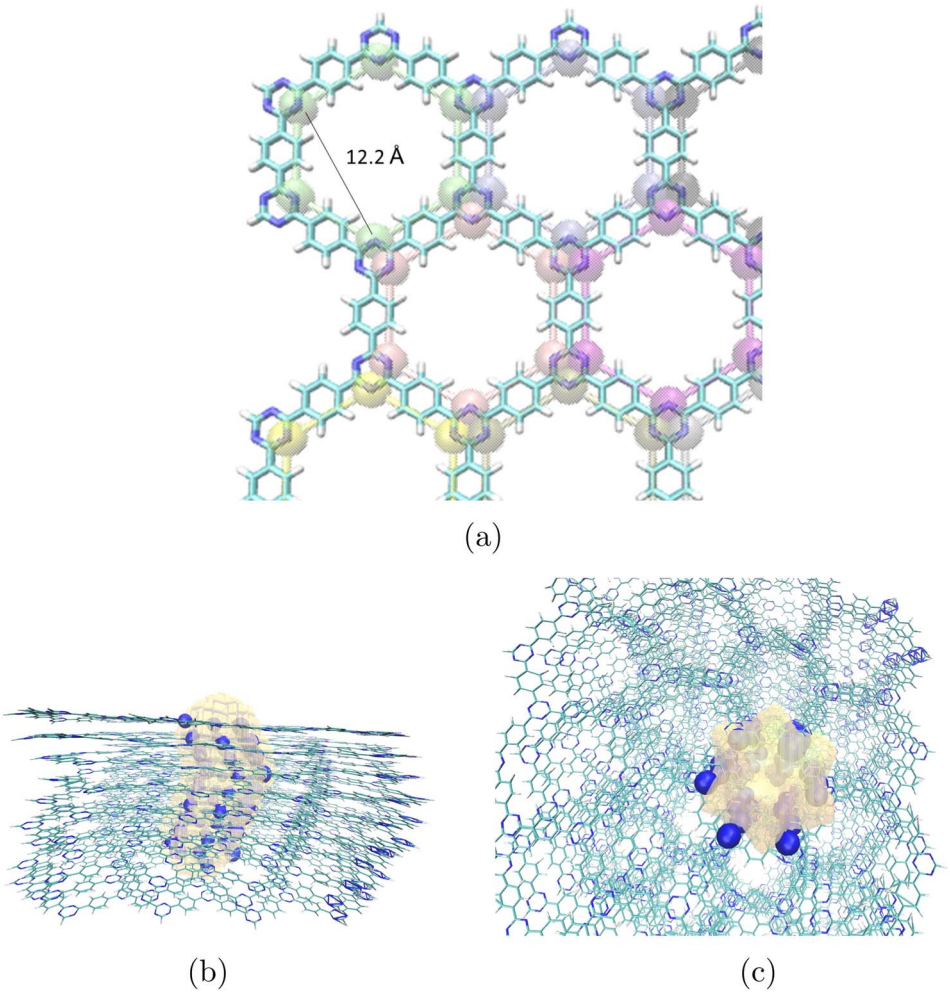

Fig. 9 The cutoff to classify pore adsorbancy is determined by the distance between the secondary neighboring nitrogens within the pore, illustrated in (a). PFAS molecule classified as adsorbed if it is within this cutoff of 4 nitrogens from the same pore and layer of a COF subsystem. The volume for a given pore is illustrated in (b) and (c).

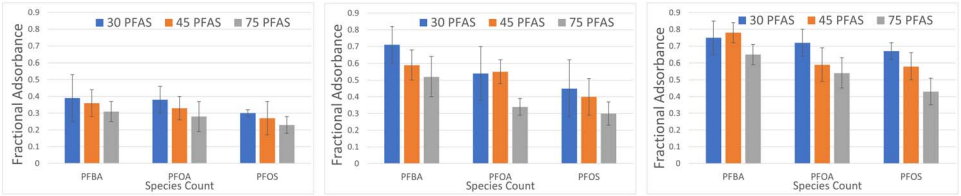

(a) CTF-FUM (b) CTF-1 (c) CTF-2

Fig. 10 Average fraction of trajectory that each PFAS species were adsorbed into respective COF subsystem, for one of the 45 PFAS trajectories: (a) CTF-FUM, (b) CTF-1, (c) CTF-2. Definition of adsorption described and illustrated in Fig. 9. The plots for all 5 trajectories are include in the supplemental material.

to the longer chained PFAS species. This result may appear contradictory to the thermodynamic results from the umbrella sampling simulations, but these results appear to arise due to the kinetic factors. PFBA would naturally have more mobility in the aqueous phase thus reaching the pores and saturating them before the longer chains defused through the aqueous phase. This kinetic result would naturally reflect the initial adsorption populations when the polluted effluent flows over the COF matrices. Earlier experimental studies, using adsorption isotherms on CTF-1, confirm that the thermodynamic results of higher PFOS and PFOA adsorption concentration were achieved as compared to their shorter chain cousins, such as PFBA.[83] Other studies have demonstrated between 80–90% PFAS removal from contaminated water with a number of CTF based COFs on the order of a few minutes, and that PFOA and PFOS were preferred at the thermodynamic limit with adsorption capacity of roughly 300 mg g^{-1}.[49,84,85] Our results show roughly double that adsorption capacity, but this is likely due to the compact nature of the model COFs used and the lack of other contaminates, such as coexisting organic matter,[104] in the aqueous phase.

In addition to the fractional adsorbance, our goal is to gauge how well PFAS is removed from the aqueous phase into the COF matrix. As such, how well a PFAS is retained within the pores becomes the next avenue of inquiry. Fig. 11 illustrates the degree of adsorption of PFAS to the 16 pores of a COF surface. The same adsorption criteria as above is used to determine the number of PFAS bound within the space of a given pore. As indicated by the previous discussion, PFAS adsorbs and remains adsorbed in the pores of the COFs, but as the pore size increases the adsorption becomes more transient. This transience is especially notable for the CTF-2 example, where Fig. 11(c) shows higher transient binding as compared to the other two COFs studied. It is also apparent in these time evolution plots that the pores have an unequal number of bound PFAS. This holds true for all of the trajectories considered in this work (see SI 3–5 for additional plots illustrating for the other trajectories). CTF-FUM has unoccupied pores while simultaneously also having doubly occupied pores, and once bound the PFAS rarely desorbed from their pores. Across the three chosen concentrations (see Table 1), CTF-1 pores were almost always bound to at least one PFAS while some pores maintained three bound PFAS. CTF-2 with its larger pore size was able to maintain up to five PFAS, but their binding as previously mentioned proves to be more transient. Overall, these three COFs demonstrate a strong capacity to remove PFAS from the aqueous phase.

In order to quantify the number and permanence of PFAS binding to these pores, we consider the retention of the PFAS in the pores. PFAS is considered retained when it is consistently bound to the COF layers (as defined above) for, at the minimum, 40% of the production trajectory. Fig. 12 presents the average

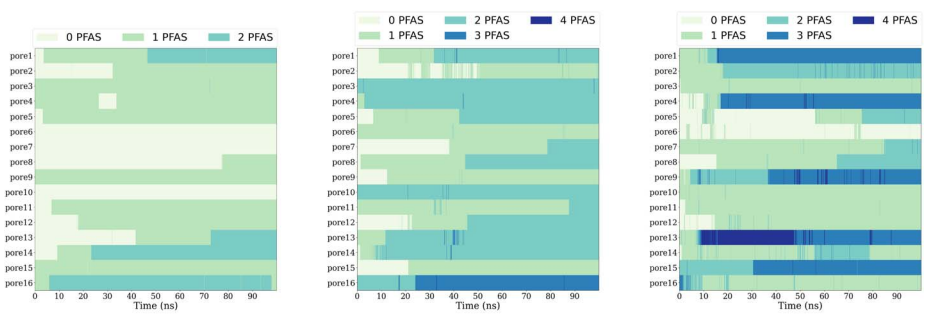

(a) CTF-FUM (b) CTF-1 (c) CTF-2

Fig. 11 Time evolution of PFAS adsorption into pores of the COF media, with 45 PFAS per unit cell: (a) CTF-FUM, (b) CTF-1, (c) CTF-2. Adsorption criteria is defined by Fig. 9 and associated discussion. Figure provides the count of the number of PFAS adsorbed to the pore, these counts are used to construct Fig. 12.

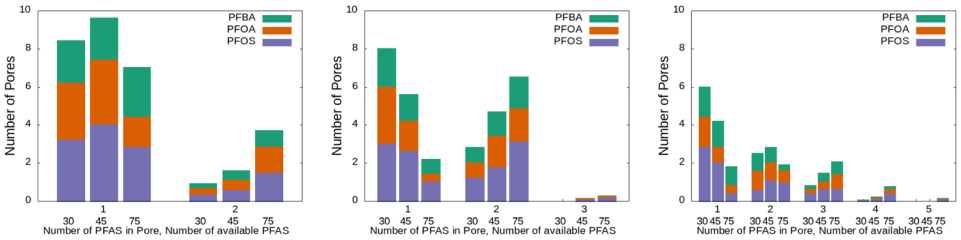

(a) CTF-FUM (b) CTF-1 (c) CTF-2

Fig. 12 Histogram of number of pores with degree of saturation, with ratio of PFAS species: (a) CTF-FUM, (b) CTF-1, (c) CTF-2. *X*-axis consists of the degree of adsorption the furture divided by the concentration as detailed in Table 1.

degree of adsorption across the 16 pores, with the five replicate trajectories, with $\mathcal{N}$ number of bound PFAS. The bar plots additionally show the relative percentage for each PFAS species. Firstly, as observed above, an increased pore size naturally allows for a higher number of PFAS to be simultaneously adsorbed into a given pore. Across all three COFs, an increase in the initial PFAS concentration in the aqueous phase leads to population shifting towards higher number of molecules adsorbing into individual pores. As the number of available PFAS increases, pores which bound a single PFAS molecule adsorbs additional PFAS, although the maximum number of PFAS adsorbed is dependent upon the pore size (Table 4). For instance, CTF-FUM can only adsorb one PFAS into each end of a pore, as there are both steric and energetic hindrances to additional PFAS adsorption. PFAS with carboxylic head groups show a significantly larger tendency to double up in the CTF-FUM pores as compared to the PFOS species, with PFBA especially prone to doubling up due to its higher mobility through the aqueous phase and smaller steric footprint. Similarly CTF-1 showed favorably of the doubling up of the two carboxylic species in the pores while PFOS were mostly singularly adsorbed. As the aqueous PFAS concentration is increased the adsorbates double or even triple up in the pores, PFBA is especially prone to this, with about half of the doubled up PFAS being PFBA in the highest concentration trajectories. This substantiates the previous results which indicate a steric and kinetic advantage for PFBA adsorption not reflected in the energetic treatment of singular PFAS adsorption. CTF-2, with its large pore size, follows the same trend of increased adsorption counts for the pores as the concentration is increased, going as high as 4 to 5 PFAS in a given pore. Although CTF-2 likely allows for higher order adsorption for PFOS species because it has a larger pore which will not create as much steric hindrance for the sulfonic head group as CTF-1 and CTF-FUM. With higher concentration, PFOS seems to show a propensity for triple adsorption into the pores. The only quintuple adsorption observed consisted of 2 PFOA and 3 PFOS absorbed into the same pore. Meanwhile PFBA in these large pores mostly remained in double adsorbed pores.

All three CTFs considered have PFAS adsorbed in over half their pores at lower concentrations and are fully saturated by 0.08 molal (or molar) concentrations of PFAS, as shown in Tables 3 and 4. As the concentration increases, the amount of PFAS adsorbed into the CTFs increases. However, as the concentration increases, so the total number of PFAS, including PFAS in aqueous solution. At 0.03 Molar concentration, CTF-1 and CTF-2 removed between 60–65% of the PFAS, which is approximately 20 PFAS molecules, from the solution. At 0.08 molar concentration, these two COFs removed between 40–45% of the PFAS which amounts to between 30-35 PFAS molecules. This indicates that there is an optimal concentration at which to use these COFs for PFAS removal. In constrast, the smallest pore, CTF-FUM, greatly under performs PFAS removal as compared to the other large pores, having roughly 2/3rds the absorption capacity, which is consistent with the previous discussions. Out of all the COFs studied herein, CTF-1 saturates the most readily and performs the best at low concentrations removing 64% of PFAS from solution. In contrast, CTF-2 has larger pores and a higher capacity for PFAS. This capacity is offset, however, because its hold on adsorbed PFAS is transient. Fig. 10 further decomposes the absorption percentages from Table 4 for each of the three PFAS species. At lower concentrations the three PFAS species are absorbed at similar rates, but as the concentration increases PFBA absorption and retention becomes more favored. In particular CTF-1 shows a remarkable 80% adsorption of PFBA at the lowest concentration, while CTF-2 shows the least selectivity of the three PFAS species. As discussed previously, PFBA absorption into these pores are not energetically favored from umbrella sampling (Table 2 and Fig. 5) or linear interaction energy (Fig. 7), so the higher

Table 3 Average number of pores saturated

COF	30PFAS	45PFAS	75PFAS
CTF-FUM	10.2	12.8	14.4
CTF-1	13.6	15.4	16.0
CTF-2	11.4	13.0	15.4

Table 4 Average number of PFAS adsorbed

COF	30PFAS	45PFAS	75PFAS
CTF-FUM	12.0 (40%)	16.0 (36%)	21.8 (29%)
CTF-1	19.2 (64%)	25.6 (57%)	30.6 (41%)
CTF-2	18.0 (60%)	22.8 (51%)	34.8 (46%)

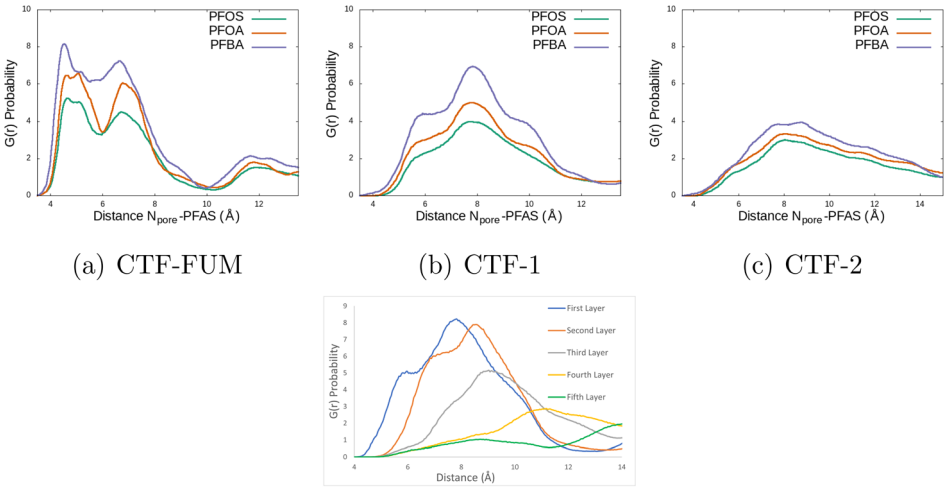

Fig. 13 Radial density functions of PFAS species in the 45 PFAS trajectories. Figure (a–c) show RDFs of terminal tail carbon of PFAS species to pore nitrogens of the COFs. (d) Captures the distance of the head group of PFOA to the nitrogen by layer depth into CTF-1 pore.

adsorption rates of PFBA are likely arising due to kinetic factors, such as the high mobility of PBFA over PFOS and PFOA. This could lead to improved competitiveness as PFBA reaches the COF surface before PFOA and PFOS.

3.3. Geometric analysis

Geometric analysis using radial distribution functions (RDFs) was also performed to examine the depth of adsorption into the pore observed with each PFAS. The RDFs shown in Fig. 13 are the pair distance probabilities between the terminal carbon of the PFAS tail to the nitrogen atoms of the pore. Panels A though C show the RDFs for each PFAS species averaged over all replicates and simulation time for CTF-FUM, CTF-1, and CTF-2 respectively. As the pore size increases, the amount of ordering and specificity for a preferred adsorption location decreased. This is evidenced by the decreasing magnitude of the peak intensities and the increasing width of those peaks. In each COF pore, PFBA RDFs show the most consistent orientation preferences, *i.e.* we see the shorter chain and quicker diffusion enable more ordered packing within the COF. Panels A–C of Fig. 13 show the average RDFs from the nitrogens of each layer of COF encompassing all pore depths. Therefore, the double peak in RDFs with CTF-FUM means that the most preferred orientation of the PFAS, which as previously discussed occurs at the mouth of the pore, is 4.5 Å away from the closest layer of COF nitrogens, and 7 Å away from the second closest outer layer and centered in the pore. The well-defined valley between the two peaks in the RDF indicates a "ratcheting" mechanism where PFAS entry will occur in somewhat discreet steps with a small barrier to further entry. CTF-1 RDFs do not contain these valleys. Instead they show an underlying 3-position surface (with critical points at approximately 6 Å, 8 Å, and 10 Å) with enough variance available in configuration space to smoothly transition from layer to layer. CTF-2 pores are large enough that no real discernible structure is observed in the RDF due to the numerous possible binding configurations that all result in different pair distances with the PFAS terminal carbon and the COF nitrogens. In panel D of Fig. 13, an example is shown for PFOA in CTF-1 with RDFs broken down by COF layer representing different depths into the pore. These are subcomponents of the overall RDF, *i.e.* the average of all five lines in panel D is what comprises the orange line of panel B. Similar behavior is observed for all three COFS and PFAS and the rest of the plots are available in the Fig. S6 through S8. All three PFAS exhibit the strongest binding (highest peak) and closest position (furthest left peak) with the first two layers of each COF pore. In the pore interior (layers 4 and 5) there is almost no probability of finding PFAS indicating that there is very limited PFAS adsorbtion deep into the pore. Additional RDF of the PFAS with the carbons that are bound to hydrogens of the linker moieties (ethylene or aryl) are provided in Fig. S9. The slight increase in RDF peak for CTF-FUM over CTF-1 and CTF-2 further demonstrates the impact of the pore size upon the adsorption of PFAS is a greater effect than the impact of the exact chemistry of the hydrophobic linker group. Overall, the RDF results shed light on where and how PFAS are adsorbing onto the COF structures, based on this information, adsorption media with pore sizes 6–10 Å in diameter is expected to be limited in PFAS sorption capacity by the number of surface pore openings it has. Therefore particle size and surface access will be critical factors in the adsorption media design for capacity. Design features to maximize selectivity towards linear and short chain PFAS appear to occur most in pore sizes around 8 Å wide.

4. Conclusion

In this paper we have investigated the impact of COF pore size on the adsorption of mixtures of straight chain PFAS molecules from the aqueous phase. These range of COF pores maintained the same effective local chemistry but varied their width

between 6 to 10 Å as inspired by the work previously done on MOFs.[73] This investigation indicates that 8 Å pore, CTF-1, occupies a goldilocks zone. Smaller pores display higher interaction energies and better hydrophobicity but are less effective due to steric and capillary effects. Meanwhile larger pores have greater volumetric capacity but lose much of the interaction energy and lessens the hydrophobic bias towards PFAS adsorption. Of the COFs examined herein, CTF-1 has optimal performance for the PFAS capture from the aqueous phase. It functions well at lower concentrations with high pore saturation even at dilute PFAS levels. As such, CTF-1 would be a great candidate for refining dilute systems to non-detection limits. The broader takeaway, from the thermodynamic calculations and molecular simulations, is that adsorpton of PFAS into COFs under dilute conditions shows promise. Additionally, there is an interplay between the thermodynamic and kinetic effects within these systems. Thermodynamic results indicate that the longer chain PFAS, PFOA and PFOS, would be the preferential sorbates into the CTF pores. Molecular dynamic simulations show a dominance of PFBA adsorption across concentrations and pore sizes. This discrepancy is due to the steric and kinetic advantage of the shorter chain PFBA, which adsorbs at a higher rate than its longer chained counterparts. As such, one would predict the short term favoring of smaller PFAS while the long term dominance of the adsorption of longer chain PFAS. This conflict between the kinetic and thermodynamic adsorption results could be leveraged to adjust selectivity in the application of COF based adsorption methods.

Author contributions

All authors were involved in the conception of the presented idea. Timothy Ricard and Timothy Schutt performed the computations and data presentation. Caitlin Bresnahan verified the results and contributed to analysis of results. Manoj Shukla supervised the findings of this work. All authors discussed the results and contributed to the final manuscript.

Conflicts of interest

There are no conflicts to declare.

Data availability

All data sets used and/or generated in this work are obtainable from the corresponding author upon reasonable request and as per our organization policy. The SI includes information on the COF structures investigated, method for PFAS-pore angle calculation, time evolution of PFAS adsorption in each COF, partitioning calculation, numerous radial distribution functions of PFAS and pore features, and analysis of the water and hydrogen bonding within each of the pore types. See DOI: **https://doi.org/10.1039/d4va00422a**.

Acknowledgements

The use of trade, product, or firm names in this report is for descriptive purposes only and does not imply endorsement by the U.S. Government. The tests described and the resulting data presented herein, unless otherwise noted, were obtained from research conducted under the Installations and Operational Environments RDA of USACE-ERDC. Permission was granted by the Chief of Engineers to publish this information. The findings of this report are not to be construed as an official Department of the Army position unless so designated by other authorized documents. This work was also supported by a grant of computer time from the DOD High Performance Computing Modernization Program at ERDC, Vicksburg. This document has been approved for public release (Distribution Statement A). This research was supported in part by an appointment to the Department of Defense (DOD) Research Participation Program administered by the Oak Ridge Institute for Science and Education (ORISE) through an interagency agreement between the U.S. Department of Energy (DOE) and the DOD. ORISE is managed by ORAU under DOE contract number DE-SC0014664. All opinions expressed in this paper are the author's and do not necessarily reflect the policies and views of DOD, DOE, or ORAU/ORISE.

References

1 N. Kudo and Y. Kawashima, Toxicity and toxicokinetics of perfluorooctanoic acid in humans and animals, *J. Toxicol. Sci.*, 2003, **28**, 49–57.
2 D. Lemal, Perspective on fluorocarbon chemistry, *J. Org. Chem.*, 2004, **69**, 1.
3 C. Lau, K. Anitole, C. Hodes, D. Lai, A. Pfahles-Hutchens and J. Seed, Perfluoroalkyl acids: A review of monitoring and toxicological findings, *Toxicol. Sci.*, 2007, **99**, 366.
4 D. Richterova, L. Fabelova, H. Patayova, J. Pulkrabova, D. Lankova, K. Rausova, E. Sovcikova, J. Stencl, J. Hajslova, T. Trnovec and L. Palkovicova Murinova, Determinants of prenatal exposure to perfluoroalkyl substances in the Slovak birth cohort, *Environ. Int.*, 2018, **121**, 1304.
5 A. Jansen, M. H. Müller, R. Grønnestad, O. Klungsøyr, A. Polder, E. Skjerve, J. Aaseth and J. L. Lyche, Decreased plasma levels of perfluoroalkylated substances one year after bariatric surgery, *Sci. Total Environ.*, 2019, **657**, 863.
6 A. Biggeri, G. Stoppa, L. Facciolo, G. Fin, S. Mancini, V. Manno, G. Minelli, F. Zamagni, M. Zamboni, D. Catelan and L. Bucchi, All-cause, cardiovascular disease and cancer mortality in the population of a large Italian area contaminated by perfluoroalkyl and polyfluoroalkyl substances (1980–2018), *Environ. Health*, 2024, **23**, 42.
7 EPA Press Office: EPA Announces It Will Keep Maximum Contaminant Levels for PFOA, PFOS, May 14, 2025, **www.epa.gov/newsreleases**.
8 USEPA, Announcement of final regulatory determinations for contaminants on the fourth drinking water contaminant candidate list, *Fed. Regist.*, 2021, **86**, 12272.

9 C. T. Vu and T. Wu, Recent progress in adsorptive removal of per-and poly-fluoroalkyl substances (PFAS) from water/wastewater, *Crit. Rev. Environ. Sci. Technol.*, 2022, **52**, 90.
10 J. O'Connor, N. S. Bolan, M. Kumar, A. S. Nitai, M. B. Ahmed, S. S. Bolan, M. Vithanage, J. Rinklebe, R. Mukhopadhyay, P. Srivastava, B. Sarkar, A. Bhatnagar, H. Wang, K. H. Siddique and M. Kirkham, Distribution, transformation and remediation of poly-and per-fluoroalkyl substances (PFAS) in wastewater sources, *Process Saf. Environ. Prot.*, 2022, **164**, 91.
11 N. Faithfull and J. Weers, Perfluorocarbon compounds, *Vox Sang.*, 1998, **74**, 243.
12 C. Lau, K. Anitole, C. Hodes, D. Lai, A. Pfahles-Hutchens and J. Seed, Perfluoroalkyl acids: a review of monitoring and toxicological findings, *Toxicol. Sci.*, 2007, **99**, 366.
13 K. Prevedouros, I. T. Cousins, R. C. Buck and S. H. Korzeniowski, Sources, fate and transport of perfluorocarboxylates, *Environ. Sci. Technol.*, 2006, **40**, 32.
14 M. Filipovic, A. Woldegiorgis, K. Norström, M. Bibi, M. Lindberg and A.-H. Österås, Historical usage of aqueous film forming foam: A case study of the widespread distribution of perfluoroalkyl acids from a military airport to groundwater, lakes, soils and fish, *Chemosphere*, 2015, **129**, 39.
15 M. Haukås, U. Berger, H. Hop, B. Gulliksen and G. W. Gabrielsen, Bioaccumulation of per-and polyfluorinated alkyl substances (PFAS) in selected species from the Barents Sea food web, *Environ. Pollut.*, 2007, **148**, 360.
16 J. W. Washington, T. M. Jenkins, K. Rankin and J. E. Naile, Decades-Scale Degradation of Commercial, Side-Chain, Fluorotelomer-Based Polymers in Soils and Water, *Environ. Sci. Technol.*, 2015, **49**, 915.
17 H. Fromme, S. A. Tittlemier, W. Voelkel, M. Wilhelm and D. Twardella, Perfluorinated compounds - Exposure assessment for the general population in western countries, *Int. J. Hyg. Environ. Health*, 2009, **212**, 239.
18 Z. Wang, I. T. Cousins, M. Scheringer, R. C. Buck and K. Hungerbühler, Global emission inventories for C4–C14 perfluoroalkyl carboxylic acid (PFCA) homologues from 1951 to 2030, Part I: production and emissions from quantifiable sources, *Environ. Int.*, 2014, **70**, 62.
19 E. M. Sunderland, X. C. Hu, C. Dassuncao, A. K. Tokranov, C. C. Wagner and J. G. Allen, A review of the pathways of human exposure to poly-and perfluoroalkyl substances (PFASs) and present understanding of health effects, *J. Exposure Sci. Environ. Epidemiol.*, 2019, **29**, 131.
20 F. Xiao, Emerging poly- and perfluoroalkyl substances in the aquatic environment: A review of current literature, *Water Res.*, 2017, **124**, 482.
21 D. Melzer, N. Rice, M. H. Depledge, W. E. Henley and T. S. Galloway, Association between serum perfluorooctanoic acid (PFOA) and thyroid disease in the US National Health and Nutrition Examination Survey, *Environ. Health Perspect.*, 2010, **118**, 686.
22 A. Shankar, J. Xiao and A. Ducatman, Perfluoroalkyl chemicals and chronic kidney disease in US adults, *Am. J. Epidemiol.*, 2011, **174**, 893.
23 C. Fei, J. K. McLaughlin, R. E. Tarone and J. Olsen, Perfluorinated chemicals and fetal growth: a study within the Danish National Birth Cohort, *Environ. Health Perspect.*, 2007, **115**, 1677.
24 U. N. Joensen, R. Bossi, H. Leffers, A. A. Jensen, N. E. Skakkebæk and N. Jørgensen, Do perfluoroalkyl compounds impair human semen quality?, *Environ. Health Perspect.*, 2009, **117**, 923.
25 V. Barry, A. Winquist and K. Steenland, Perfluorooctanoic acid (PFOA) exposures and incident cancers among adults living near a chemical plant, *Environ. Health Perspect.*, 2013, **121**, 1313.
26 K. Steenland and S. Woskie, Cohort mortality study of workers exposed to perfluorooctanoic acid, *Am. J. Epidemiol.*, 2012, **176**, 909.
27 K. Steenland, T. Fletcher and D. A. Savitz, Epidemiologic Evidence on the Health Effects of Perfluorooctanoic Acid (PFOA), *Environ. Health Perspect.*, 2010, **118**, 1100.
28 K. Matsumoto, M. Kubota, H. Matsuoka and H. Yamaoka, Water-soluble fluorine-containing amphiphilic block copolymer: synthesis and aggregation behavior in aqueous solution, *Macromolecules*, 1999, **32**, 7122–7127.
29 N. Ghosh, S. Roy and J. A. Mondal, On the Behavior of Perfluorinated Persistent Organic Pollutants (POPs) at Environmentally Relevant Aqueous Interfaces: An Interplay of Hydrophobicity and Hydrogen Bonding, *Langmuir*, 2020, **36**, 3720.
30 J. R. Robalo, L. M. Streacker, D. M. de Oliveira, P. Imhof, D. Ben-Amotz and A. V. Verde, Hydrophobic but Water-Friendly: Favorable Water-Perfluoromethyl Interactions Promote Hydration Shell Defects, *J. Am. Chem. Soc.*, 2019, **141**, 15856.
31 E. Clot, O. Eisenstein, N. Jasim, S. A. Macgregor, J. E. McGrady and R. N. Perutz, C- F and C- H bond activation of fluorobenzenes and fluoropyridines at transition metal centers: how fluorine tips the scales, *Acc. Chem. Res.*, 2011, **44**, 333.
32 M. E. Evans, C. L. Burke, S. Yaibuathes, E. Clot, O. Eisenstein and W. D. Jones, Energetics of C- H bond activation of fluorinated aromatic hydrocarbons using a complex, [Tp Rh (CNneopentyl)] complex, *J. Am. Chem. Soc.*, 2009, **131**, 13464.
33 J. C. Biffinger, H. W. Kim and S. G. DiMagno, The polar hydrophobicity of fluorinated compounds, *ChemBioChem*, 2004, **5**, 622.
34 S. Roy, B. Biswas, N. Ghosh, P. C. Singh and J. A. Mondal, Hydrophobic Hydration of Fluoroalkyl (C-F) is Distinctly Different from That of Its Hydrogenated Counterpart (C-H), as Observed by Raman Difference with Simultaneous Curve Fitting Analysis, *J. Phys. Chem. C*, 2019, **123**, 27012.
35 L. Silvani, G. Cornelissen, A. B. Smebye, Y. Zhang, G. Okkenhaug, A. R. Zimmerman, G. Thune, H. Saevarsson and S. E. Hale, Can biochar and designer biochar be used to remediate per-and polyfluorinated

alkyl substances (PFAS) and lead and antimony contaminated soils?, *Sci. Total Environ.*, 2019, **694**, 133693.
36 K. Luo, Y. Pang, D. Wang, X. Li, L. Wang, M. Lei, Q. Huang and Q. Yang, A critical review on the application of biochar in environmental pollution remediation: Role of persistent free radicals (PFRs), *J. Environ. Sci.*, 2021, **108**, 201.
37 E. Sørmo, L. Silvani, N. Bjerkli, N. Hagemann, A. R. Zimmerman, S. E. Hale, C. B. Hansen, T. Hartnik and G. Cornelissen, Stabilization of PFAS-contaminated soil with activated biochar, *Sci. Total Environ.*, 2021, **763**, 144034.
38 K. M. Krahn, G. Cornelissen, G. Castro, H. P. H. Arp, A. G. Asimakopoulos, R. Wolf, R. Holmstad, A. R. Zimmerman and E. Sørmo, Sewage sludge biochars as effective PFAS-sorbents, *J. Hazard. Mater.*, 2023, **445**, 130449.
39 S. Lath, D. A. Navarro, D. Losic, A. Kumar and M. J. McLaughlin, Sorptive remediation of perfluorooctanoic acid (PFOA) using mixed mineral and graphene/carbon-based materials, *Environ. Chem.*, 2018, **15**, 472.
40 X. Jiang, W. Wang, G. Yu and S. Deng, Contribution of nanobubbles for PFAS adsorption on graphene and OH- and NH2-functionalized graphene: Comparing simulations with experimental results, *Environ. Sci. Technol.*, 2021, **55**, 13254.
41 C. G. Bresnahan, T. C. Schutt and M. K. Shukla, Exploration of functionalizing graphene and the subsequent impact on PFAS adsorption capabilities via molecular dynamics, *Chemosphere*, 2023, **345**, 140462.
42 Z. Du, S. Deng, S. Zhang, B. Wang, J. Huang, Y. Wang, G. Yu and B. Xing, Selective and high sorption of perfluorooctanesulfonate and perfluorooctanoate by fluorinated alkyl chain modified montmorillonite, *J. Phys. Chem. C*, 2016, **120**, 16782.
43 S. E. Hearon, A. A. Orr, H. Moyer, M. Wang, P. Tamamis and T. D. Phillips, Montmorillonite clay-based sorbents decrease the bioavailability of per-and polyfluoroalkyl substances (PFAS) from soil and their translocation to plants, *Environ. Res.*, 2022, **205**, 112433.
44 C. M. Luft, T. C. Schutt and M. K. Shukla, Properties and Mechanisms for PFAS Adsorption to Aqueous Clay and Humic Soil Components, *Environ. Sci. Technol.*, 2022, **56**, 10053.
45 A. Maimaiti, S. Deng, P. Meng, W. Wang, B. Wang, J. Huang, Y. Wang and G. Yu, Competitive adsorption of perfluoroalkyl substances on anion exchange resins in simulated AFFF-impacted groundwater, *Chem. Eng. J.*, 2018, **348**, 494.
46 Y.-L. Liu and M. Sun, Ion exchange removal and resin regeneration to treat per-and polyfluoroalkyl ether acids and other emerging PFAS in drinking water, *Water Res.*, 2021, **207**, 117781.
47 F. Dixit, R. Dutta, B. Barbeau, P. Berube and M. Mohseni, PFAS removal by ion exchange resins: A review, *Chemosphere*, 2021, **272**, 129777.
48 D. Abdullatif, A. Khosropour, A. Khojastegi, I. Mosleh, L. Khazdooz, A. Zarei and A. Abbaspourrad, Triazine-and Heptazine-Based Porous Organic Polymer Networks for the Efficient Removal of Perfluorooctanoic Acid, *ACS Appl. Polym. Mater.*, 2022, **5**, 412.
49 G. Liu, X. Wei, P. Luo, S. Dai, W. Zhang and Y. Zhang, Novel fluorinated nitrogen-rich porous organic polymer for efficient removal of perfluorooctanoic acid from water, *Water*, 2022, **14**, 1010.
50 S. Deng, Y. Nie, Z. Du, Q. Huang, P. Meng, B. Wang, J. Huang and G. Yu, Enhanced adsorption of perfluorooctane sulfonate and perfluorooctanoate by bamboo-derived granular activated carbon, *J. Hazard. Mater.*, 2015, **282**, 150.
51 N. Saeidi, F.-D. Kopinke and A. Georgi, Understanding the effect of carbon surface chemistry on adsorption of perfluorinated alkyl substances, *Chem. Eng. J.*, 2020, **381**, 122689.
52 P. S. Pauletto and T. J. Bandosz, Activated carbon versus metal-organic frameworks: A review of their PFAS adsorption performance, *J. Hazard. Mater.*, 2022, **425**, 127810.
53 U. Ghosh, R. G. Luthy, G. Cornelissen, D. Werner and C. A. Menzie, In-situ Sorbent Amendments: A New Direction in Contaminated Sediment Management, *Environ. Sci. Technol.*, 2011, **45**, 1163.
54 S. E. Hale, H. P. H. Arp, G. A. Slinde, E. J. Wade, K. Bjørseth, G. D. Breedveld, B. F. Straith, K. G. Moe, M. Jartun and Å. Høisæter, Sorbent amendment as a remediation strategy to reduce PFAS mobility and leaching in a contaminated sandy soil from a Norwegian firefighting training facility, *Chemosphere*, 2017, **171**, 9.
55 P. Meng, S. Deng, X. Lu, Z. Du, B. Wang, J. Huang, Y. Wang, G. Yu and B. Xing, Role of air bubbles overlooked in the adsorption of perfluorooctanesulfonate on hydrophobic carbonaceous adsorbents, *Environ. Sci. Technol.*, 2014, **48**, 13785.
56 Q. Yu, R. Zhang, S. Deng, J. Huang and G. Yu, Sorption of perfluorooctane sulfonate and perfluorooctanoate on activated carbons and resin: Kinetic and isotherm study, *Water Res.*, 2009, **43**, 1150.
57 S. Deng, Q. Yu, J. Huang and G. Yu, Removal of perfluorooctane sulfonate from wastewater by anion exchange resins: Effects of resin properties and solution chemistry, *Water Res.*, 2010, **44**, 5188.
58 H. Furukawa, N. Ko, Y. B. Go, N. Aratani, S. B. Choi, E. Choi, A. Ö. Yazaydin, R. Q. Snurr, M. O'Keeffe, J. Kim and O. M. Yaghi, Ultrahigh porosity in metal-organic frameworks, *Science*, 2010, **329**, 424.
59 H. Deng, S. Grunder, K. E. Cordova, C. Valente, H. Furukawa, M. Hmadeh, F. Gándara, A. C. Whalley, Z. Liu, S. Asahina, H. Kazumori, M. O'Keeffe, O. Terasaki, J. F. Stoddart and O. M. Yaghi, Large-pore apertures in a series of metal-organic frameworks, *Science*, 2012, **336**, 1018.
60 P. Li, N. A. Vermeulen, C. D. Malliakas, D. A. Gómez-Gualdrón, A. J. Howarth, B. L. Mehdi, A. Dohnalkova,

N. D. Browning, M. O'Keeffe and O. K. Farha, Bottom-up construction of a superstructure in a porous uranium-organic crystal, *Science*, 2017, **356**, 624.

61 Z. Chen, P. Li, R. Anderson, X. Wang, X. Zhang, L. Robison, L. R. Redfern, S. Moribe, T. Islamoglu, D. A. Gómez-Gualdrón, T. Yildirim, J. F. Stoddart and O. K. Farha, Balancing volumetric and gravimetric uptake in highly porous materials for clean energy, *Science*, 2020, **368**, 297.

62 S.-Y. Ding and W. Wang, Covalent organic frameworks (COFs): from design to applications, *Chem. Soc. Rev.*, 2013, **42**, 548.

63 N. Huang, P. Wang and D. Jiang, Covalent organic frameworks: a materials platform for structural and functional designs, *Nat. Rev. Mater.*, 2016, **1**, 1.

64 T. Yan, Y. Lan, M. Tong and C. Zhong, Screening and Design of Covalent Organic Framework Membranes for CO2/CH4 Separation, *ACS Sustain. Chem. Eng.*, 2019, **7**, 1220.

65 I. Ahmed and S. H. Jhung, Covalent organic framework-based materials: Synthesis, modification, and application in environmental remediation, *Coord. Chem. Rev.*, 2021, **441**, 213989.

66 A. P. Cote, A. I. Benin, N. W. Ockwig, M. O'Keeffe, A. J. Matzger and O. M. Yaghi, Porous, crystalline, covalent organic frameworks, *Science*, 2005, **310**, 1166.

67 N. Huang, P. Wang and D. Jiang, Covalent organic frameworks: a materials platform for structural and functional designs, *Nat. Rev. Mater.*, 2016, **1**, 1.

68 N. Zhang, A. Ishag, Y. Li, H. Wang, H. Guo, P. Mei, Q. Meng and Y. Sun, Recent investigations and progress in environmental remediation by using covalent organic framework-based adsorption method: A review, *J. Cleaner Prod.*, 2020, **277**, 123360.

69 K. Liu, S. Zhang, X. Hu, K. Zhang, A. Roy and G. Yu, Understanding the Adsorption of PFOA on MIL-101(Cr)-Based Anionic-Exchange Metal–Organic Frameworks: Comparing DFT Calculations with Aqueous Sorption Experiments, *Environ. Sci. Technol.*, 2015, **49**, 8657.

70 M.-J. Chen, A.-C. Yang, N.-H. Wang, H.-C. Chiu, Y.-L. Li, D.-Y. Kang and S.-L. Lo, Influence of crystal topology and interior surface functionality of metal-organic frameworks on PFOA sorption performance, *Microporous Mesoporous Mater.*, 2016, **236**, 202.

71 K. Sini, D. Bourgeois, M. Idouhar, M. Carboni and D. Meyer, Metal–organic framework sorbents for the removal of perfluorinated compounds in an aqueous environment, *New J. Chem.*, 2018, **42**, 17889.

72 R. Li, S. Alomari, R. Stanton, M. C. Wasson, T. Islamoglu, O. K. Farha, T. M. Holsen, S. M. Thagard, D. J. Trivedi and M. Wriedt, Efficient Removal of Per- and Polyfluoroalkyl Substances from Water with Zirconium-Based Metal–Organic Frameworks, *Chem. Mater.*, 2021, **33**, 3276.

73 T. S. Erkal, N. Shamsuddin, S. Kirmizialtin and A. O. Yazaydin, Computational investigation of structure–function relationship in fluorine-functionalized MOFs for PFOA capture from water, *J. Phys. Chem. C*, 2023, **127**, 3204.

74 W. Ji, L. Xiao, Y. Ling, C. Ching, M. Matsumoto, R. P. Bisbey, D. E. Helbling and W. R. Dichtel, Removal of GenX and perfluorinated alkyl substances from water by amine-functionalized covalent organic frameworks, *J. Am. Chem. Soc.*, 2018, **140**, 12677.

75 M. Zhang, J. Li, C. Zhang, Z. Wu, Y. Yang, J. Li, F. Fu and Z. Lin, In-situ synthesis of fluorinated magnetic covalent organic frameworks for fluorinated magnetic solid-phase extraction of ultratrace perfluorinated compounds from milk, *J. Chromatogr. A*, 2020, **1615**, 460773.

76 W. Wang, Z. Zhou, H. Shao, S. Zhou, G. Yu and S. Deng, Cationic covalent organic framework for efficient removal of PFOA substitutes from aqueous solution, *Chem. Eng. J.*, 2021, **412**, 127509.

77 X. Song, R. Wang, X. Wang, H. Han, Z. Qiao, X. Sun and W. Ji, An amine-functionalized olefin-linked covalent organic framework used for the solid-phase microextraction of legacy and emerging per-and polyfluoroalkyl substances in fish, *J. Hazard. Mater.*, 2022, **423**, 127226.

78 S.-Y. Ding and W. Wang, Covalent organic frameworks (COFs): from design to applications, *Chem. Soc. Rev.*, 2013, **42**, 548.

79 P. Kuhn, M. Antonietti and A. Thomas, Porous, covalent Triazine-Based Frameworks Prepared by Ionothermal Synthesis, *Angew. Chem., Int. Ed.*, 2008, **47**, 3450.

80 K. Wang, H. Huang, D. Liu, C. Wang, J. Li and C. Zhong, Covalent Triazine-Based Frameworks with Ultramicropores and High Nitrogen Contents for Highly Selective CO2 Capture, *Environ. Sci. Technol.*, 2016, **50**, 4869.

81 M. J. Bojdys, J. Jeromenok, A. Thomas and M. Antonietti, Rational Extension of the Family of Layered, Covalent, Triazine-Based Frameworks with Regular Porosity, *Adv. Mater.*, 2010, **22**, 2202.

82 B. Wang, L. S. Lee, C. Wei, H. Fu, S. Zheng, Z. Xu and D. Zhu, Covalent triazine-based framework: A promising adsorbent for removal of perfluoroalkyl acids from aqueous solution, *Environ. Pollut.*, 2016, **216**, 884.

83 W. Wang, H. Shao, C. Sun, X. Jiang, S. Zhou, G. Yu and S. Deng, Preparation of magnetic covalent triazine frameworks by ball milling for efficient removal of PFOS and PFOA substitutes from water, *Environ. Sci.: Nano*, 2022, **9**, 1466.

84 Y. Chen, X. Zhang, J. Ma, J. Gong, W. A, X. Huang, P. Li, Z. Xie, G. Li and Q. Liao, All-in-one strategy to construct bifunctional covalent triazine-based frameworks for simultaneous extraction of per- and polyfluoroalkyl substances and polychlorinated naphthalenes in foods, *J. Hazard. Mater.*, 2024, **465**, 133084.

85 W. Gong, M. Gong, G. Xiao, R. Zhang, X. Zhu, D. Li, S. Zhou and W. Wang, Fluorinated covalent triazine frameworks for highly efficient removal of per- and polyfluoroalkyl substances in water: Synthesis, performance and mechanism, *Sep. Purif. Technol.*, 2025, **361**, 131633.

86 J. Liu, E. Zong, H. Fu, S. Zheng, Z. Xu and D. Zhu, Adsorption of aromatic compounds on porous covalent

triazine-based framework, *J. Colloid Interface Sci.*, 2012, **372**, 99.

87 J. Bangma, J. McCord, N. Giffard, K. Buckman, J. Petali, C. Chen, D. Amparo, B. Turpin, G. Morrison and M. Strynar, Analytical method interferences for perfluoropentanoic acid (PFPeA) and perfluorobutanoic acid (PFBA) in biological and environmental samples, *Chemosphere*, 2023, **315**, 137722.

88 X. Min and Y. Wang, Enhanced adsorption of short-chain perfluorobutanoic acid by functionalized periodic mesoporous organosilica: Performance and mechanisms, *J. Hazard. Mater.*, 2023, **449**, 131047.

89 D. Case, H. Aktulga, K. Belfon, I. Ben-Shalom, J. Berryman, S. Brozell, D. T. E. Cerutti, I. Cheatham, G. Cisneros, V. Cruzeiro, T. Darden, N. Forouzesh, M. Ghazimirsaeed, G. Giambaşu, T. Giese, M. Gilson, H. Gohlke, A. Goetz, J. Harris, Z. Huang, S. Izadi, S. Izmailov, K. Kasavajhala, M. Kaymak, A. Kovalenko, T. Kurtzman, T. Lee, P. Lim, Z. Li, C. Lin, J. Liu, T. Luchko, R. Luo, M. Machado, M. Manathunga, K. Merz, Y. Miao, O. Mikhailovskii, G. Monard, H. Nguyen, K. O'Hearn, A. Onufriev, F. Pan, S. Pantano, A. Rahnamoun, D. Roe, A. Roitberg, C. Sagui, S. Schott-Verdugo, A. Shajan, J. Shen, C. Simmerling, N. Skrynnikov, J. Smith, J. Swails, R. Walker, J. Wang, J. Wang, X. Wu, Y. Wu, Y. Xiong, Y. Xue, D. York, C. Zhao, Q. Zhu and P. Kollman, *Amber 2024*, University of California, San Francisco, 2024.

90 L. Martínez, R. Andrade, E. G. Birgin and J. M. Martínez, PACKMOL: A package for building initial configurations for molecular dynamics simulations, *J. Comput. Chem.*, 2009, **30**, 2157.

91 W. L. Jorgensen, J. Chandrasekhar, J. D. Madura, R. W. Impey and M. L. Klein, Comparison of simple potential functions for simulating liquid water, *J. Chem. Phys.*, 1983, **79**, 926.

92 H. W. Horn, W. C. Swope, J. W. Pitera, J. D. Madura, T. J. Dick, G. L. Hura and T. Head-Gordon, Development of an improved four-site water model for biomolecular simulations: TIP4P-Ew, *J. Chem. Phys.*, 2004, **120**, 9665.

93 H. W. Horn, W. C. Swope and J. W. Pitera, Characterization of the TIP4P-Ew water model: Vapor pressure and boiling point, *J. Chem. Phys.*, 2005, 123.

94 J. Wang, R. M. Wolf, J. W. Caldwell, P. A. Kollman and D. A. Case, Development and testing of a general amber force field, *J. Comput. Chem.*, 2004, **25**, 1157.

95 J. Wang, W. Wang, P. A. Kollman and D. A. Case, Automatic atom type and bond type perception in molecular mechanical calculations, *J. Mol. Graphics Modell.*, 2006, **25**, 247.

96 M. J. Frisch, M. Head-Gordon and J. A. Pople, A direct MP2 gradient method, *Chem. Phys. Lett.*, 1990, **166**, 275.

97 R. A. Kendall, J. Dunning, H. Thom and R. J. Harrison, Electron affinities of the first-row atoms revisited. Systematic basis sets and wave functions, *J. Chem. Phys.*, 1992, **96**, 6796.

98 M. Head-Gordon and T. Head-Gordon, Analytic MP2 frequencies without fifth-order storage. Theory and application to bifurcated hydrogen bonds in the water hexamer, *Chem. Phys. Lett.*, 1994, **220**, 122.

99 M. J. Frisch, G. W. Trucks, H. B. Schlegel, G. E. Scuseria, M. A. Robb, J. R. Cheeseman, G. Scalmani, V. Barone, G. A. Petersson, H. Nakatsuji, X. Li, M. Caricato, A. V. Marenich, J. Bloino, B. G. Janesko, R. Gomperts, B. Mennucci, H. P. Hratchian, J. V. Ortiz, A. F. Izmaylov, J. L. Sonnenberg, D. Williams-Young, F. Ding, F. Lipparini, F. Egidi, J. Goings, B. Peng, A. Petrone, T. Henderson, D. Ranasinghe, V. G. Zakrzewski, J. Gao, N. Rega, G. Zheng, W. Liang, M. Hada, M. Ehara, K. Toyota, R. Fukuda, J. Hasegawa, M. Ishida, T. Nakajima, Y. Honda, O. Kitao, H. Nakai, T. Vreven, K. Throssell, J. A. Montgomery Jr, J. E. Peralta, F. Ogliaro, M. J. Bearpark, J. J. Heyd, E. N. Brothers, K. N. Kudin, V. N. Staroverov, T. A. Keith, R. Kobayashi, J. Normand, K. Raghavachari, A. P. Rendell, J. C. Burant, S. S. Iyengar, J. Tomasi, M. Cossi, J. M. Millam, M. Klene, C. Adamo, R. Cammi, J. W. Ochterski, R. L. Martin, K. Morokuma, O. Farkas, J. B. Foresman and D. J. Fox, *Gaussian16 Revision C.01*, Gaussian Inc., Wallingford CT, 2016.

100 T. C. Schutt, G. A. Hegde, V. S. Bharadwaj, A. J. Johns and C. M. Maupin, Impact of water-dilution on the solvation properties of the ionic liquid 1-methyltriethoxy-3-ethylimidazolium acetate for model biomass molecules, *J. Phys. Chem. B*, 2017, **121**, 843.

101 M. Tong, Y. Lan, Q. Yang and C. Zhong, Exploring the structure-property relationships of covalent organic frameworks for noble gas separations, *Chem. Eng. Sci.*, 2017, **168**, 456.

102 W. Humphrey, A. Dalke and K. Schulten, VMD: visual molecular dynamics, *J. Mol. Graphics*, 1996, **14**, 33.

103 P. A. Kollman, Free energy calculations: Applications to chemical and biochemical phenomena, *Chem. Rev.*, 1993, **93**, 2395.

104 E. Gagliano, M. Sgroi, P. P. Falciglia, F. G. Vagliasindi and P. Roccaro, Removal of poly-and perfluoroalkyl substances (PFAS) from water by adsorption: Role of PFAS chain length, effect of organic matter and challenges in adsorbent regeneration, *Water Res.*, 2020, **171**, 115381.